

# Steering Directional Light Emission and Mode Chirality through Postshaping of Cavity Geometry

Jiawei Wang, Min Tang, Yue-De Yang,\* Yin Yin, Yan Chen, Christian Niclaas Saggau, Minshen Zhu, Xiaobo Yuan, Dmitriy Karnaushenko, Yong-Zhen Huang, Libo Ma,\* and Oliver G. Schmidt

Dielectric optical microcavities have been explored as an excellent platform to manipulate the light flow and investigate non-Hermitian physics in open optical systems. For whispering gallery mode optical microcavities, modifying the rotational symmetry is highly desirable for intriguing phenomena such as degenerated chiral modes and directional light emission. However, for the state-of-the-art approaches, namely deforming the cavity geometry by precision lithography or introducing local scatterers near the cavity boundary via micromanipulation, there is a lack of flexibility in fine-adjusting of chiral symmetry and far-field emission direction. Here, precise engineering of cavity boundary using electron-beam-induced deposition is reported based on rolled-up nanomembrane-enabled spiral-shaped microcavities. The deformation of outer boundary results in delicate tailoring of asymmetric backscattering between the outer and inner rolling edges, and hence deterministically strong mode chirality. Besides, the crescent-shaped high-index nanocap leads to modified light tunneling channels and inflected far-field emission angle. It is envisioned that such a localized deposition-assisted technique for adjusting the structural deformation of 3D optical microcavities will be highly useful for understanding rich insights in non-Hermitian photonics and unfolding exotic properties on lasing, sensing, and cavity quantum electrodynamics.

## 1. Introduction

Whispering gallery mode (WGM) optical microcavities have been extensively studied due to their extraordinary capabilities of confining and manipulating light in deliberately designed microstructures,<sup>[1]</sup> which enables great possibilities in fundamental studies such as light-matter interactions,<sup>[2,3]</sup> non-Hermitian photonics<sup>[4–6]</sup> as well as highly diverse applications including photonic,<sup>[7]</sup> optoelectronic,<sup>[8]</sup> optofluidic,<sup>[9]</sup> and optomechanical devices.<sup>[10]</sup> The conventional WGM cavities in a circular shape support co-propagating of clockwise (CW) and counterclockwise (CCW) light-waves and orthogonal mode families.<sup>[4]</sup> Therefore, breaking the chiral symmetry, namely the local balance between the amplitudes of CW and CCW propagating waves, is of great significance for controlling the light flow and emission. Such an accomplishment indicates great potentials in broad applications such as unidirectional emission light sources,<sup>[11–13]</sup>

Dr. J. Wang, Dr. M. Tang, Dr. Y. Yin, Dr. Y. Chen, C. N. Saggau, M. Zhu, Dr. D. Karnaushenko, Dr. L. Ma, Prof. O. G. Schmidt  
Institute for Integrative Nanosciences  
Leibniz IFW Dresden, Helmholtzstraße 20, Dresden 01069, Germany  
E-mail: l.ma@ifw-dresden.de  
Prof. Y.-D. Yang, Prof. Y.-Z. Huang  
State Key Laboratory of Integrated Optoelectronics  
Institute of Semiconductors  
Chinese Academy of Sciences  
Beijing 100083, China  
E-mail: yd@semi.ac.cn

Dr. Y. Yin  
School of Materials Science and Engineering  
Jiangsu University  
Zhenjiang 212013, China  
Prof. X. Yuan  
School of Physics and Electronics  
Shandong Normal University  
Shandong 250014, China  
Dr. J. Wang, Prof. O. G. Schmidt  
Material Systems for Nanoelectronics  
Technische Universität Chemnitz  
Chemnitz 09111, Germany  
Dr. J. Wang, Prof. O. G. Schmidt  
Research Center for Materials  
Architectures and Integration of Nanomembranes (MAIN)  
Technische Universität Chemnitz  
Rosenbergstr. 6 Chemnitz 09126, Germany

 The ORCID identification number(s) for the author(s) of this article can be found under <https://doi.org/10.1002/lpor.202000118>

© 2020 The Authors. Published by Wiley-VCH GmbH. This is an open access article under the terms of the Creative Commons Attribution-NonCommercial License, which permits use, distribution and reproduction in any medium, provided the original work is properly cited and is not used for commercial purposes.

DOI: [10.1002/lpor.202000118](https://doi.org/10.1002/lpor.202000118)

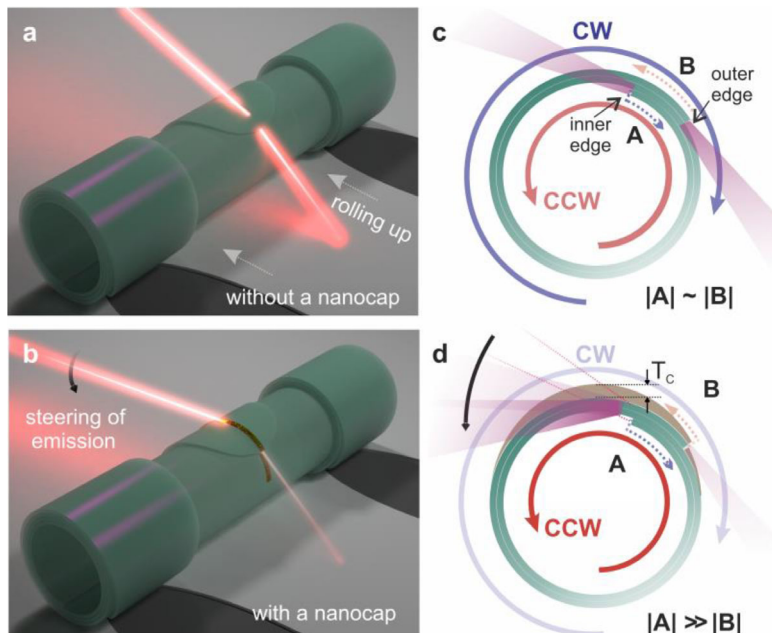


**Figure 1.** Schematics of steering the directional emission and mode chirality in a spiral nanomembrane cavity by a deposited nanobelt using EBID. Rolled-up nanomembrane as a WGM microtubular cavity: a) without a deposited nanobelt, b) with the nanobelt across the tube forming a nanocap. Schematics in a cross-sectional view showing the unbalanced backscattering between CW and CCW components and corresponding emission directions: c) without the deposited cap, d) with the cap. The thickness at the cap center is defined as  $T_c$ .

optical gyroscopes,<sup>[14,15]</sup> and single nanoparticle detections.<sup>[16–18]</sup> In conventional 2D microcavities (e.g., microdisks and microtoroids), two strategies of perturbing the cavity boundary and introducing mutual coupling between the mode pairs have been investigated. One is to design the structural geometry with broken rotational symmetry, for instance, spiral-shaped microdisks with distinct left- and right-handed forms<sup>[19–21]</sup> and limaçon cavities.<sup>[22,23]</sup> The other one is to fine adjust external nanotips close to the rim as local scatterers or absorbers and reach a coalescence of eigenmodes, termed “exceptional point.”<sup>[18,24,25]</sup> However, the first strategy suggests a rigid control on the mode chirality and directional emission properties that are locked after lithography-based patterning of the cavity geometry. The second strategy requires external and precision micromanipulation as “temporary” tuning, and does not pose a robust trimming on the cavity itself. In this context, a flexible and straightforward route to control the light flow and emission properties is highly desirable.

Recently, 3D WGM microcavities with a promoted degree of freedom for light propagation and confinement such as microtubes,<sup>[26,27]</sup> microbottles<sup>[28,29]</sup> and microbubbles<sup>[30]</sup> are attracting increasing research attention and enabling promising opportunities on single-mode lasing,<sup>[28]</sup> spin-orbit coupling,<sup>[31]</sup> photonic molecules,<sup>[32,33]</sup> and photon-plasmon coupling.<sup>[34]</sup> The realization 3D deformed WGM microcavities for studies of chiral photonics and directional light emission becomes a vigorously pursued goal. Recently, a unique spiral-shaped 3D WGM microcavity with broken structural symmetry based on self-rolled-up nanomembranes has been reported. Mode-dependent directional light emission is revealed due to the interaction between the 3D optical resonances and spatially varying rolling edges.<sup>[35]</sup>

Notably, the WGM orbits in nanomembrane-based deformed cavities are perpendicular to the plane of the substrate surface,

which potentially enables a new control knob of WGMs by engineering the boundary (e.g., the cross-sectional geometry of spiral-shaped cavities) using regular tools such as postdepositions. Here the deformation of a WGM microcavity becomes adjustable for the first time by the postfabrication electron-beam-induced deposition (EBID) as a direct writing method. A fabricated high-index nanobelt disturbs the spiral tube wall as an additional crescent-shaped nanocap structure on top of the outer rolling edge, which in turn modifies the local scatterer condition and leads to reinforced asymmetry of backscattering between CW and CCW lightwaves. Besides, the new “composite” spiral nanomembrane cavity exhibits progressive steering of the far-field emission angle due to the modified tunneling channel for light out-coupling. We experimentally achieved on-demand tunable directional emission with the angle steering up to  $\approx 30^\circ$  upon a deposited cap thickness of 15 nm. Moreover, a polarization-dependent tuning of directional emission has been presented for both experimental and simulation results. The localized deposition offers a new pathway for engineering structural deformation of optical microcavities and manipulating the resonance properties including mode energy, chirality, and external light emission profiles.

## 2. Results and Discussions

### 2.1. Working Principle

**Figure 1a,b** schematically illustrates a nanomembrane-based optical microcavity before and after the EBID process. The well-defined spiral-shaped cross-section of nanomembrane after self-rolling naturally supports WGM resonances.<sup>[35]</sup> The

ultrathin cavity wall thickness ( $\approx 260$  nm for the sample under test) suggests a strong evanescent field and hence sensitive response to a deposited layer of only a few nm thick. The pair of resonant modes can be described using simple  $2 \times 2$  non-Hermitian and nonsymmetric matrices<sup>[19]</sup>

$$H = \begin{pmatrix} E_0 & 0 \\ 0 & E_0 \end{pmatrix} + \begin{pmatrix} \Gamma & A \\ B & \Gamma \end{pmatrix} \quad (1)$$

where the eigenvectors of the first matrix describe the equal CCW(CW) components in a circular cavity and the second matrix presents the effect of two rolling edges in the spiral nanomembrane (see Figure 1c). The diagonal elements are given by the out-coupling rates (assumed to be the same for simplicity here). The complex-valued off-diagonal elements  $A$  and  $B$  are the backscattering coupling coefficients.  $A$  ( $B$ ) describes the backscattering from the CW (CCW) to the CCW (CW) components. The complex eigenvalues are

$$E_{\pm} = E_0 + \Gamma \pm \sqrt{AB} \quad (2)$$

and the complex (not normalized) eigenvectors are

$$\psi_{\pm} = \begin{pmatrix} \sqrt{A} \\ \pm \sqrt{B} \end{pmatrix} \quad (3)$$

Therefore the mode chirality can be defined as

$$\alpha = 1 - \frac{\min(|\psi_{CCW}|^2, |\psi_{CW}|^2)}{\max(|\psi_{CCW}|^2, |\psi_{CW}|^2)} = 1 - \frac{\min(|A|, |B|)}{\max(|A|, |B|)} \quad (4)$$

In spite of the intrinsic structural chirality in spiral nanomembranes for breaking the balance of CW and CCW lightwaves ( $|\psi_{CCW}| \neq |\psi_{CW}|$ ), the two rolling edges with same heights may still lead to comparable backscattering strengths, e.g.,  $|A| \approx |B|$ . As illustrated in Figure 1c, probabilistic bi-directional emission with comparable intensities can be established due to the out-coupling effect of both outer and inner rolling edges. The “upper” emission beam is contributed by the tunneling of the CCW component and back-reflected CW component at the inner edge. And the “lower” emission beam is caused by the tunneling of the CW component and back-reflected CCW component at the outer edge.

Various post-fabrication resonance tuning schemes for on-chip integrated planar WGM cavities have been investigated, which mainly focus on the real part of mode energies.<sup>[36–41]</sup> Among them, EBID as a convenient and precise tool has been employed for generating additional 3D nanostructures, such as nanopillars on top of microdisks<sup>[42]</sup> and photonic crystals.<sup>[43]</sup> In the EBID method, released gaseous molecules get decomposed under the irradiation of a focused electron beam, resulting in the growth of nonvolatile structures on the focus site. Therefore, it enables accurate patterning of a crescent-shaped nanobelt on top of the tube surface (Figure 1d). While previous reports focus on post-fabrication EBID-based modifications of planar photonic devices with localized defects or scatterers, our scheme offers a new pathway of fine re-shaping the cavity morphology. The high-index crescent-shaped nanocap leads to a deformed spiral structure with a modified outer boundary. The composite spiral

cavity with an asymmetric cap varies resonant light leakage sites along the rim and consequently the emission directions. Besides, the nanocap-decorated outer rolling edge renders the outer edge as the foremost scatter rather than a combined effect from two edges, and further breaks the balance between  $|A|$  and  $|B|$  (e.g.,  $|A| \gg |B|$ , see Figure 1d). A strong mode chirality emerges while the CCW lightwave becomes the dominant component. Consequently, a deterministic unidirectional-like emission formed by the upper lobe is expected with a tuned emission angle.

## 2.2. Numerical Simulations

In order to visualize the resonant modes upon engineered deformation, 2D numerical simulations using the finite-element method were carried out (see the Experimental Section and Figure S1, Supporting Information). For a bare spiral nanomembrane cavity with radius  $R = 6$   $\mu\text{m}$  and an effective refractive index  $n_{\text{eff}}$  of  $\approx 1.6$ , the simulated electric-field distribution for transverse-magnetic (TM, defined as the electric field parallel to the tube axis) polarization suggests a regular WGM feature (Figure 2a). The resonant fields of standing wave suggest comparable spatial overlapping with the inner and outer rolling edges (Figure 2b). In the far-field emission profile in Figure 2c, the rolling edges lead to deterministic out-coupling of resonant light to far-field along the orientation of the edge facets. Two discerned main emission lobes are labeled as the principal lobe ( $L_p$ , with highest peak intensity) centered at  $\approx 45^\circ$  and the second principal lobe ( $L_s$ , with second-highest peak intensity) centered at  $\approx 210^\circ$ .

By introducing a high-index cap layer ( $n \approx 2.4$ ), the mode distribution along the radial dimension gets shifted away from the inner edge toward the new outer boundary modified by the deposited carbon belt (see Figure 2d,e). Hence the “collision” effect at the outer rolling edge is enhanced compared to the original case, while the interaction with the inner edge gets suppressed. The opposite effects on two edges give rise to a strong asymmetry of backscattering between CW and CCW components. The extracted intensity polar plot suggests a clear rotation of emission angle for  $L_p$  ( $\approx 32^\circ$  for  $T_C = 15$  nm and  $\approx 80^\circ$  for  $T_C = 30$  nm in Figure 2c). Moreover, unidirectional emission appears with a negligible  $L_s$  for  $T_C = 30$  nm, which is in sharp contrast to those of  $T_C = 0$  and 15 nm.

The weight of CW and CCW components for the internal optical mode field can be quantified by considering the simulated mode field distribution versus the angular momentum index  $m$  by

$$\psi_z(\rho, \varphi) = \sum_{m=-\infty}^{\infty} f_m(\rho) e^{im\varphi} \quad (5)$$

where  $\rho$  and  $\varphi$  are the polar coordinates, and the positive (negative) values of  $m$  represent the CCW (CW) propagating mode components.<sup>[13]</sup> So the normalized intensity can be calculated by

$$I_m = \int_0^{\infty} |f_m(\rho)|^2 \rho d\rho \quad (6)$$

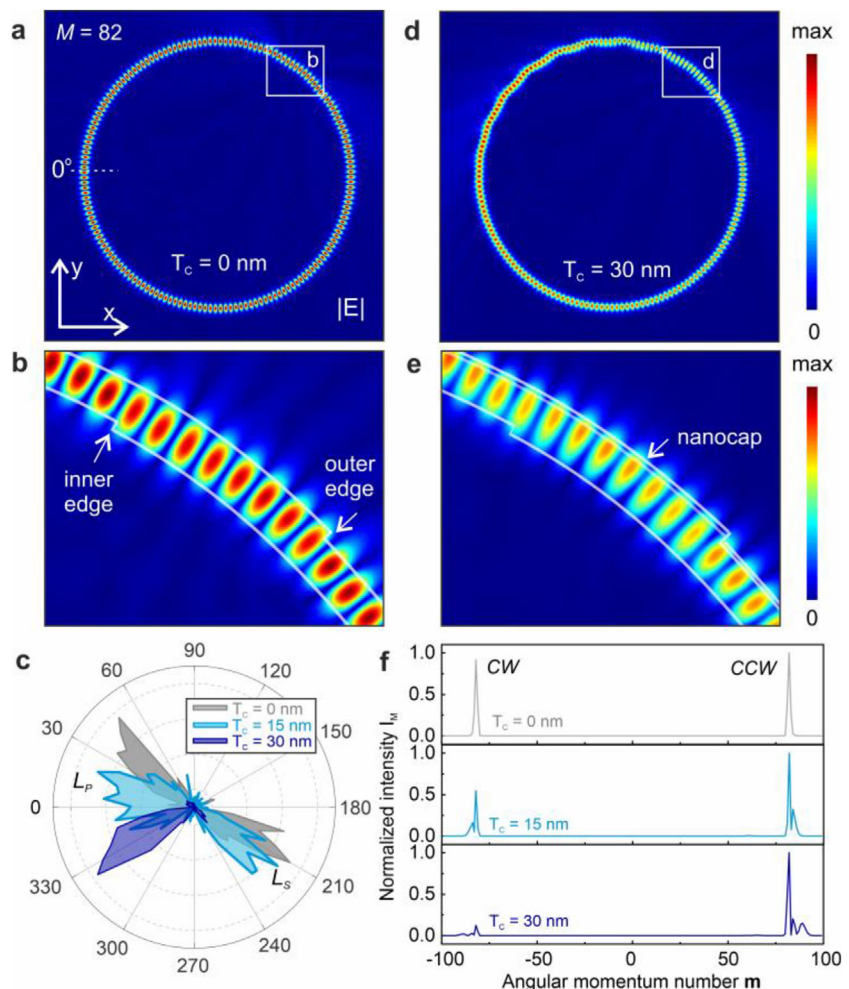


**Figure 2.** Simulation results for a spiral nanomembrane cavity without and with the nanocap-induced modification. Simulated electric field amplitude distribution for TM mode at the azimuthal mode order  $M = 82$ : a)  $T_c = 0 \text{ nm}$ , d)  $T_c = 30 \text{ nm}$ . b,e) Zoomed-in view around the inner and outer rolling edges for (a) and (c), respectively. c) Polar plot of the far-field emission intensity. f) Calculated normalized intensity distributions versus angular momentum number  $m$ .

Therefore, the mode chirality can be calculated based on the extracted normalized intensity for CW and CCW components by

$$\alpha = 1 - \frac{\min(\sum_{m=-\infty}^{-1} I_m, \sum_{m=1}^{\infty} I_m)}{\max(\sum_{m=-\infty}^{-1} I_m, \sum_{m=1}^{\infty} I_m)} \in (0, 1) \quad (7)$$

For the bare spiral nanomembrane cavity in Figure 2a, comparable  $I_m$  for CW and CCW components with a low chirality of  $\approx 0.07$  are obtained (see Figure 2f), which is consistent with the two emission lobes with comparable intensities in Figure 2b. After introducing the nanocap with  $T_c$  of 15 and 30 nm, a clear difference of  $I_m$  for CW and CCW components appears and the chirality is gradually lifted to  $\approx 0.82$ . The increasing weight of CCW traveling-wave leads to a strengthened  $L_p$  and simultaneously a weakened  $L_s$ , approaching unidirectional emission shown in Figure 2c. Upon a detuned winding number  $W$ , the mode chirality of a bare spiral cavity oscillates due to the constructive and destruc-

tive interference of the CW/CCW lightwave and back-reflected CCW/CW lightwave at the edges<sup>[35,44]</sup> and results in probabilistic bi-directional or unidirectional emission. Here, owing to the elevated mode chirality by a deposited cap, a deterministic unidirectional emission is preserved (see Text S1 and Figure S2, Supporting Information).

To better understand the steering mechanism of emission angles in Figure 2c, Husimi function-based analysis was employed as a useful tool for correlating mode field distributions with emission properties in phase space.<sup>[35]</sup> For the bare spiral nanomembrane cavity, comparable CCW and CW components with opposite  $\sin(\chi)$  are mainly distributed out of the leaky region (see Figure 3a). As indicated in the leaky region for the bare cavity in Figure 3b, the light leakage forming two far-field emission beams is discerned around the azimuthal positions of two edges. In contrast, a much stronger CCW component rather than the CW component is revealed for  $T_c = 30 \text{ nm}$  (see Figure 3c), which agrees well with the results in Figure 2f. In Figure 3d, the distribution of the CCW component shifts from the inner edge ( $\approx 120^\circ$ )

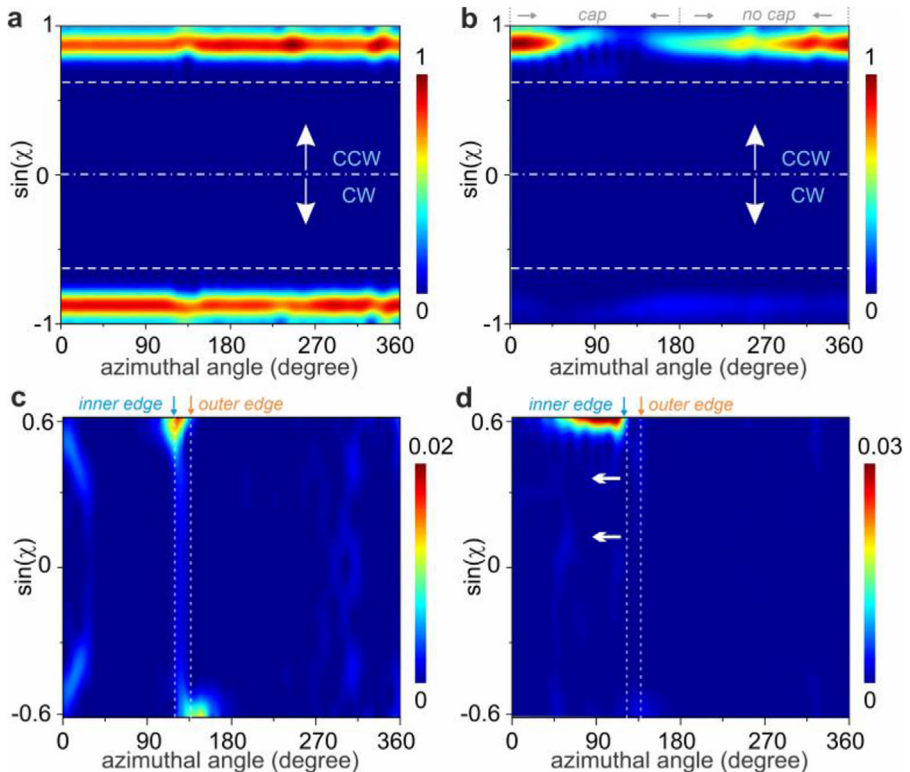


**Figure 3.** Visualization of light out-coupling channels using Husimi function. The calculated internal emerging Husimi functions at the outer boundary of the spiral nanomembrane cavity: a)  $T_C = 0 \text{ nm}$ , c)  $T_C = 30 \text{ nm}$ . The critical angles for total internal reflection in the bare spiral nanomembrane layer ( $1/n_{\text{eff}} \approx 0.6$ ) are indicated by the white dashed lines. The area between two dashed lines is termed as the leaky region. The positive region ( $\sin(\chi) > 0$ ) stands for CCW components while the negative region ( $\sin(\chi) < 0$ ) stands for CW components. b,d) Zoomed-in view of the leaky region for (a) and (c).

to the nanocap region ( $\approx 60^\circ$ – $105^\circ$ ), which verifies that the leakage mechanism is no longer dominated by the inner edge but strongly dependent on the high-index cladding profile. The relatively thick cap at the central top surface enables a stronger capability of lightwave guiding, and hence light escapes at a bent direction compared to the facet orientation of the inner edge, which explains the rotation of emission angle for  $L_p$  in Figure 2c.

### 2.3. Experimental Characterizations of Selective Perturbations

In experiments, SiO/SiO<sub>2</sub> bilayer nanomembrane-based microtubular cavities were fabricated via the rolled-up technique (see the Experimental Section). The EBID process was repeated five times with a deposited thickness of  $\approx 3 \text{ nm}$  in each round (see Figure S3, Supporting Information). Here amorphous carbon was chosen as the deposited material due to the mature process with a low impurity<sup>[45]</sup> compared with others (e.g., metals<sup>[46]</sup>) and the high refractive index contrast between the formed nanocap and the nanomembrane cavity. The scanning electron microscopy (SEM) image in Figure 4a reveals the deposited nanobelt aligned at the center of the parabolic-shaped segment of the rolled-up microtube. The “exserted” nanomembrane segment in Figure 4a induces additional optical confinement along the axial direction, behaving as a parabolic-shaped optical quasi-potential well.<sup>[26]</sup> The single resonant mode splits into fundamental and high order axial modes  $E_q$  ( $q$  is the axial mode number), which can be

theoretically modeled by solving the wave equation in an optical quasi-potential well (see the upper left panel of Figure 4b).<sup>[26,47]</sup>

The presence of the 600 nm wide high-index nanobelt at the center of the “exserted” nanomembrane segment essentially modifies the quasi-potential well, and in turn, modulates the axial modes that spatially overlap with the nanobelt. In the numerical modeling, an increased averaged  $n_{\text{eff}}$  of the nanomembrane layer at the central region estimated by perturbation theory<sup>[48]</sup> is employed to treat the impact of the 15 nm thick carbon nanobelt, which results in a localized “dip” at the center of the quasi-potential well (see Text S2, Supporting Information). This dip at the potential well interacts strongly with the fundamental mode  $E_0$  (see the upper right panel of Figure 4b) as they spatially overlap with each other. On the contrary, the other axial modes, especially the even modes (e.g., the first and third order modes  $E_1$  and  $E_3$ ) are less affected due to the weak mode overlapping.

Resonant spectra were collected using a microphotoluminescence ( $\mu$ PL) measurement setup (see the Experimental Section). Defects in the amorphous silicon oxide nanomembrane layer exhibit a broadband emission profile ranging from  $\approx 1.5$  to  $\approx 2.5 \text{ eV}$ .<sup>[49]</sup> Measured resonant spectra for TM and transverse-electric (TE, electric fields perpendicular to the tube axis) modes in Figure 4c show clear sets of higher-order axial modes with almost equal spectral mode spacing, which is attributed to the parabolic shape of the quasi-potential well.<sup>[26,47]</sup> In the spatially resolved mapping results (see the lower panel of Figure 4b), axial modes exhibit distinctive mode field

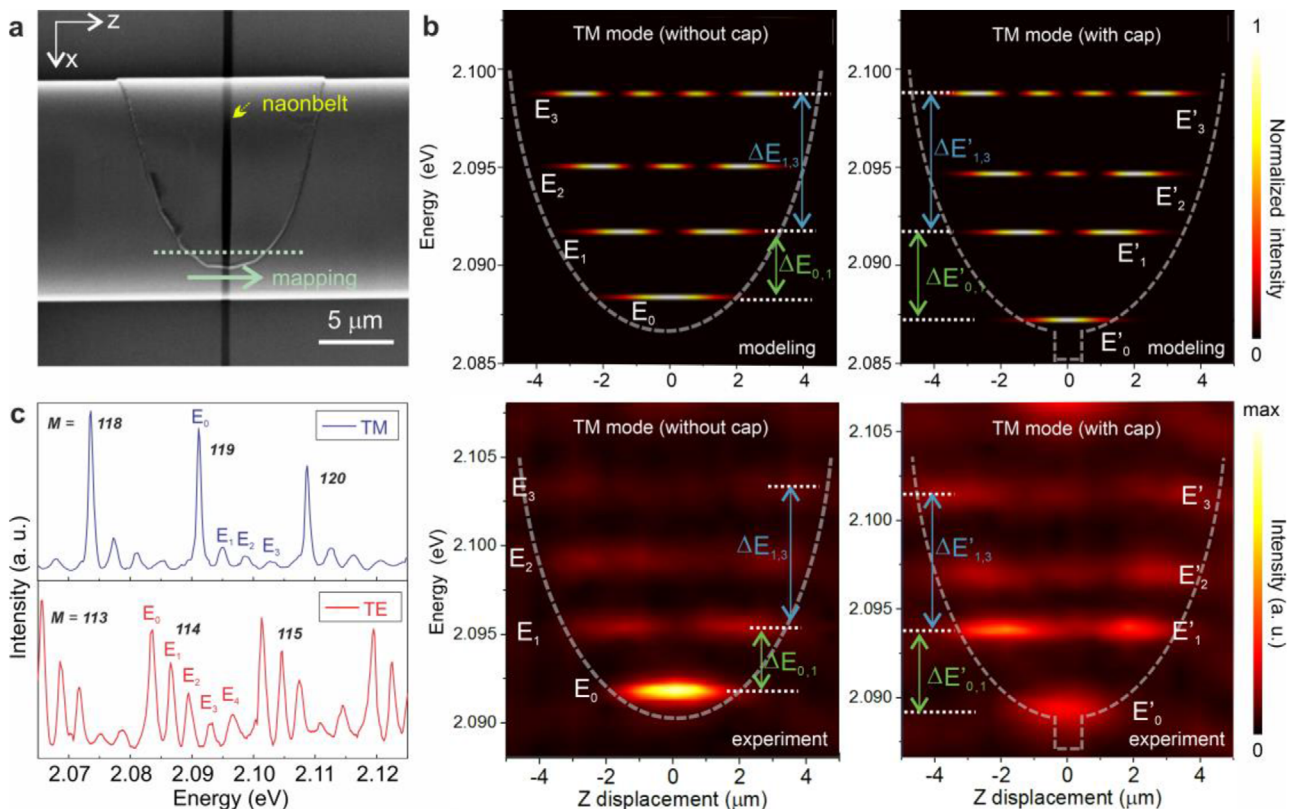


**Figure 4.** Characterization of a spiral nanomembrane microtubular cavity upon EBID-based tuning. a) SEM image of the central region after depositing a nanocap at the center of the parabolic segment. The microtube has a diameter of 14.4  $\mu\text{m}$  and winding number  $W$  of  $\approx 3.1$ . Light green dots indicate the measurement sites for the mapping along the axial direction. b) Upper panels: modeled eigenenergies and associated spatial intensity distributions of  $E_0$ - $E_3$  for  $T_C = 0 \text{ nm}$  (left) and  $15 \text{ nm}$  (right). According to the number of mode antinodes along the axial direction, they can be divided into odd modes ( $E_0$  and  $E_2$ ) and even modes ( $E_1$  and  $E_3$ ). Lower panels: spatially and energetically resolved PL images for  $T_C = 0 \text{ nm}$  (left) and  $15 \text{ nm}$  (right). The gray dashed lines denote the optical quasi-potential wells. c) Measured resonant spectra for both TM and TE modes.

distributions around the center (denoted as  $z = 0$ ). The axial mode spacing  $\Delta E_{0,1}$  between  $E_0$  and  $E_1$  becomes much widened after introducing the nanobelt, which is attributed to the effective spectral tuning on  $E_0$  but a much weaker interaction to  $E_1$ . It is shown that the overall change of  $\Delta E_{0,1}$  for TE mode (44%, see Figures S4 and S5, Supporting Information) is much higher than that for TM mode ( $\approx 18\%$ ). This agrees with the higher surface sensitivity of TE mode to the deposited nanocap rather than that of TM mode. In contrast, the mode spacing  $\Delta E_{1,3}$  between two even modes  $E_1$  and  $E_3$  shows a minor change ( $\approx 4\%$  for TM mode and  $\approx 9\%$  for TE mode, see Figure S6, Supporting Information), which proves the selective perturbation on the mode energies.

#### 2.4. Nanocap-Induced Steering Effect

The far-field emission profiles of the fundamental mode after each round of deposition for both polarizations were recorded by angle-resolved measurements (see Figure 5a,b). Continuous rotation of the emission angle from  $\approx 60^\circ$  to  $\approx 30^\circ$  for TM mode is obtained upon the gradually increased  $T_C$  (see Figure 5a). As summarized in Figure 5c, the smooth tuning suggests an efficiency as

the slope of  $\approx 2^\circ$  per nm. Besides, the directional emission feature is nicely preserved with an averaged full width at half-maximum (FWHM) divergence angle of  $\approx 15^\circ \pm 4^\circ$  throughout the process. However, a distinct behavior for TE mode in Figure 5d shows that the emission angle fluctuates in a sophisticated trend. The single emission lobe first splits into two lobes and then re-combines for  $T_C = 9 \text{ nm}$ .

Simulation results of  $L_p$  in TM mode suggest a rotation of emission angle  $\approx 32^\circ$  for  $T_C = 15 \text{ nm}$  and  $\approx 68^\circ$  for  $T_C = 30 \text{ nm}$  (see Figure 5e). The extracted slope of  $\approx 2.4^\circ$  per nm is consistent with the experimental results. Remarkably, the emission angle for  $L_s$  is much less affected ( $\approx 19^\circ$  for  $T_C = 30 \text{ nm}$ , see Figure S7, Supporting Information), which suggests that  $L_s$  is still strongly dependent on the outer rolling edge. In contrast, a minor effect for both  $L_p$  and  $L_s$  in TE mode is shown with a rotation of  $\approx 3^\circ$  for  $T_C = 30 \text{ nm}$  (in Figure 5f), which seems somewhat counterintuitive as the mode energies suggest a much stronger modulation rather than that of TM mode (see Figure S7, Supporting Information). The nanocap does not lead to an intense TE-polarized mode field trapped inside the high-index crescent-shaped region (see Figure S8, Supporting Information). Hence, the original light emission mechanism is much less perturbed compared to that of TM mode, which explains the inefficient tuning of directional emissions.

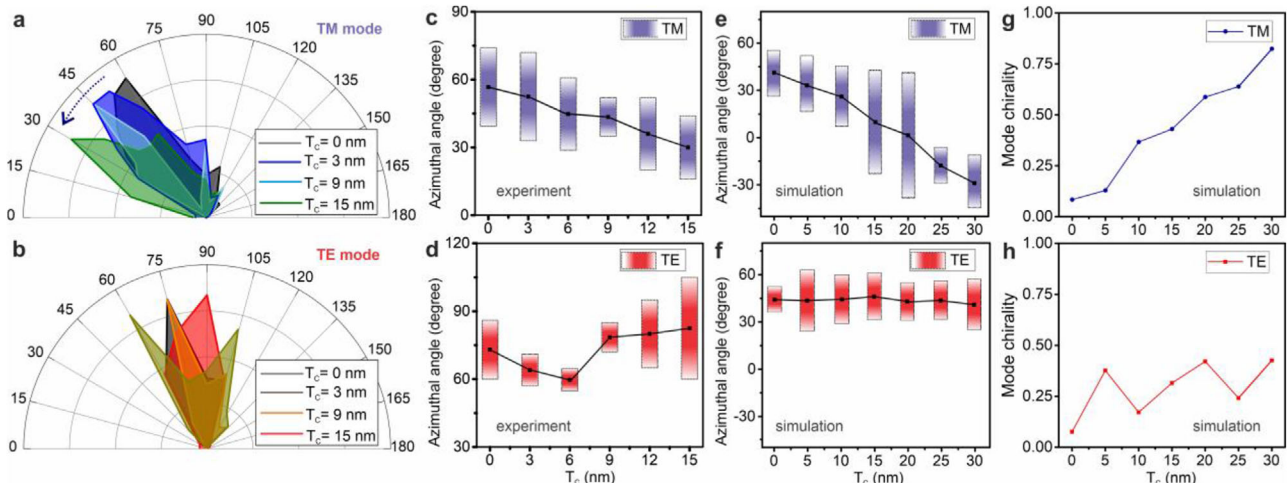


**Figure 5.** Measured and simulated results on steering directional emission and mode chirality. Measured polar plots of the normalized far-field emission intensity upon different  $T_c$  for a) TM and b) TE modes. Summarized emission angle of the primary lobe as a function of  $T_c$  for c) TM and d) TE modes. Bars indicate the FWHM divergence angles. Simulated emission angle as a function of  $T_c$  for e) TM and f) TE modes. Calculated mode chirality for g) TM and h) TE modes.

Figure 5g,h summarizes the calculated mode chirality for different  $T_c$ . The increasing value (i.e., enhanced CCW component) from 0.07 to 0.82 for TM mode leads to an improved weight of  $L_p$  and hence gradually approaches the unidirectional emission regime (Figure S9, Supporting Information). The mode chirality for TE mode fluctuates between 0.08 and 0.42. The overall low value agrees with the emission with bi-direction-like emission with a poor unidirectionality (Figure S9, Supporting Information).

### 3. Conclusion

In summary, we have proposed and systematically investigated a new strategy of re-shaping the cavity boundary for manipulating the properties of 3D optical resonances in a spiral nanomembrane cavity, including mode energy, mode chirality, and directional light emission. Through localized patterning of an amorphous carbon nanobelt as a high-index cap on top of the rolled-up nanomembrane, both the cavity outer boundary and the localized scatterer condition get modified progressively. The transition between CW and CCW traveling-wave components and the light out-coupling channels into the far-fields get significantly modified for TM resonant modes. Besides, the polarization-dependent effect is obtained with a significantly weakened tuning of directional emission and mode chirality for TE modes. Such a scheme is not limited to curved nanomembranes but also can be applied to other 3D optical microcavities and photonic devices. The precise structural deformation via boundary engineering serves as an unprecedented control knob for exploring rich insights in non-Hermitian photonics such as wave chaos, spin-orbit coupling, PT-symmetry breaking, etc. We envision that the steered optical devices acquiring exotic properties will potentially open up new concepts and possibilities in light sources, sensors, and photonic integrated circuits.<sup>[50]</sup>

### 4. Experimental Section

**Numerical Simulations:** 2D numerical simulations were performed based on the finite-element method (COMSOL Multiphysics wave-optics module, see Figure S1, Supporting Information). The cross-sectional cavity shape was defined using the standard spiral function following the previous publications (radius  $R = 6 \mu\text{m}$ , deformation parameter  $\epsilon = 0.01$ ).<sup>[35]</sup> The winding number  $W$  (defined as the rolling length divided by the circumference)  $\approx 3.1$  and angular position of two rolling edges were set according to the characterized sample by SEM inspection. The regular meshing size was set as 20 nm. Fine meshing was applied to regions around the nanocap with a size of  $\approx 0.2$  nm. The effective refractive indices  $n_{\text{eff}}$  of the nanomembrane layer and cap layer were set as 1.6 and  $2.4 + 0.7i$ , respectively.<sup>[51]</sup> Circular-shaped perfect matching layers as the outmost boundary were introduced for simulating the mode field distribution. The far-field emission profile was extracted as the power outflow at the boundary of the background medium (air) as a function of the azimuthal angle. The two calculated nearly degenerate modes were nonorthogonal and shared the same chirality. Here the mode with a relatively higher Q factor was analyzed and presented in the article. The emerging Husimi function was calculated following the previous methods with the extracted electric mode fields in the simulation as inputs.<sup>[35]</sup>

**Sample Fabrication:** Nanomembrane-based tubular microcavities were fabricated following the previous experiences.<sup>[32]</sup> A  $2 \mu\text{m}$  thick photoresist layer (ARP-3510, Allresists GmbH) was patterned on a thermal oxide-coated silicon substrate by a maskless photolithography process (MLA 100, Heidelberg Instruments). A U-shape pattern was adopted to ensure a free-standing middle section after rolling up, which largely suppresses the substrate leakage loss and preserves a reasonably high Q factor  $\approx 10^3$ – $10^4$  (see Figure S1, Supporting Information).<sup>[52]</sup> Bilayer nanomembrane ( $20 \text{ nm SiO}$  and  $40 \text{ nm SiO}_2$ ) was fabricated by electron-beam deposition (Edwards Auto500 e-beam evaporator) at a glancing angle of  $60^\circ$ . The difference of deposition rate from  $5 \text{ \AA s}^{-1}$  ( $\text{SiO}$ ) to  $0.5 \text{ \AA s}^{-1}$  ( $\text{SiO}_2$ ) leads to differentially strained layers. Then the photoresist layer was dissolved in dimethyl sulfoxide (DMSO) to trigger the rolling-up process. A critical point dryer (931 GL, Tousimis CPD) was employed during the evaporation of solvents to avoid the collapse of rolled-up microtubular structures. At last, a homogenous coating of  $40 \text{ nm}$  thick  $\text{Al}_2\text{O}_3$  layer was performed by atomic layer deposition (FLEXAL, Oxford Instruments) for improving the optical confinement.

EBID was performed using an SEM (Zeiss Crossbeam 550). The precursor gas was delivered around the deposition area via a gas injection

system inside the SEM chamber. The deposition area was defined as  $\approx 20 \mu\text{m}$  (long)  $\times 600 \text{ nm}$  (wide). The calibrated deposition rate was  $\approx 1 \text{ \AA s}^{-1}$  upon an acceleration voltage of 20 kV. The EBID was repeated for 5 times ( $\approx 30 \text{ s}$  for each round) at the same site upon the same dose. The nanobelt thickness was examined by atomic force microscopy (Dimension 3100 Nanoman, Veeco).

**Optical Characterizations:** Resonant emission spectra were collected using a  $\mu\text{PL}$  confocal setup (LabRAM HR Evolution, Horiba). A continuous-wave laser beam at 457 nm (Cobolt Twist) was focused onto the tube top surface using a long-working-distance objective lens (Olympus LMPLFLN 50 $\times$ ) with a measuring distance of  $\approx 11 \text{ mm}$  and a spot size  $\approx 1 \mu\text{m}^2$ . The power of laser excitation onto the sample was adjusted to  $\approx 0.2 \text{ mW}$  to avoid any heat-induced damage to the structure. The emission signal was collected by the same objective lens and analyzed by a spectrometer with 600 blz  $\text{mm}^{-1}$ . The polarization state was determined using a rotatable half-wave plate and a fixed polarization analyzer. The sample was mounted first on a rotational stage then onto a motorized translational stage. Spatially resolved measurements were conducted by scanning along the tube axis (z-axis) with a scanning step of  $0.5 \mu\text{m}$  and collecting the far-field emission signals. Angle-resolved measurements were conducted with a step of  $7.5^\circ$  (around the high-intensity region) or  $15^\circ$  (around the low-intensity region).

## Supporting Information

Supporting Information is available from the Wiley Online Library or from the author.

## Acknowledgements

The authors thank Ronny Engelhard, Stefan Baunack, and Yuhao Wu for technical support. This work was supported by the German Research Foundation DFG (SCHM 1298/26-1 and SCHM 1298/22-1). The authors acknowledge financial support from the DFG through Würzburg-Dresden Cluster of Excellence on Complexity and Topology in Quantum Matter—ct.qmat (EXC 2147, project-ID 390858490). Y.-D.Y. thanks the support from the Natural Science Foundation of China NSFC (Grant 61875188). Y.Y. thanks the support from the National Natural Science Foundation of China (Grant 11904138) and the Natural Science Foundation of Jiangsu Province (BK20190837).

## Conflict of Interest

The authors declare no conflict of interest.

## Keywords

chirality, curved nanomembranes, directional emission, electron-beam-induced deposition, whispering gallery mode

Received: March 26, 2020

Revised: June 10, 2020

Published online: September 11, 2020

- [1] S. Yang, Y. Wang, H. Sun, *Adv. Opt. Mater.* **2015**, *3*, 1136.
- [2] C. Junge, D. O'shea, J. Volz, A. Rauschenbeutel, *Phys. Rev. Lett.* **2013**, *110*, 213604.
- [3] S. Frustaci, F. Vollmer, *Curr. Opin. Chem. Biol.* **2019**, *51*, 66.
- [4] H. Cao, J. Wiersig, *Rev. Mod. Phys.* **2015**, *87*, 61.

- [5] R. El-Ganainy, K. G. Makris, M. Khajavikhan, Z. H. Musslimani, S. Rotter, D. N. Christodoulides, *Nat. Phys.* **2018**, *14*, 11.
- [6] Q. Zeng, E. Lafalce, C. H. Lin, M. J. Smith, J. Jung, Y. Yoon, Z. Lin, V. V. Tsukruk, Z. V. Vardeny, *Nano Lett.* **2019**, *19*, 6049.
- [7] T. Reynolds, N. Riesen, A. Meldrum, X. Fan, J. M. M. Hall, T. M. Monro, A. François, *Laser Photonics Rev.* **2017**, *11*, 1600265.
- [8] Z. Yao, K. Wu, B. X. Tan, J. Wang, Y. Li, Y. Zhang, A. W. Poon, *IEEE J. Sel. Top. Quantum Electron.* **2018**, *24*, 5900324.
- [9] Y.-N. Zhang, T. Zhou, B. Han, A. Zhang, Y. Zhao, *Nanoscale* **2018**, *10*, 13832.
- [10] H. Xiong, Y. Wu, *Appl. Phys. Rev.* **2018**, *5*, 031305.
- [11] Q. Song, L. Ge, A. Stone, H. Cao, J. Wiersig, J.-B. Shim, J. Unterhinninghofen, W. Fang, G. Solomon, *Phys. Rev. Lett.* **2010**, *105*, 103902.
- [12] X. F. Jiang, C. L. Zou, L. Wang, Q. Gong, Y. F. Xiao, *Laser Photonics Rev.* **2016**, *10*, 40.
- [13] S.-S. Sui, Y.-Z. Huang, M.-Y. Tang, Y.-D. Yang, J.-L. Xiao, Y. Du, *IEEE J. Sel. Top. Quantum Electron.* **2016**, *23*, 1500308.
- [14] L. Ge, R. Sarma, H. Cao, *Optica* **2015**, *2*, 323.
- [15] R. Sarma, L. Ge, J. Wiersig, H. Cao, *Phys. Rev. Lett.* **2015**, *114*, 053903.
- [16] J. Wiersig, *Phys. Rev. Lett.* **2014**, *112*, 203901.
- [17] N. Zhang, Z. Gu, S. Liu, Y. Wang, S. Wang, Z. Duan, W. Sun, Y.-F. Xiao, S. Xiao, Q. Song, *Optica* **2017**, *4*, 1151.
- [18] W. Chen, S. K. Özdemir, G. Zhao, J. Wiersig, L. Yang, *Nature* **2017**, *548*, 192.
- [19] J. Wiersig, S. W. Kim, M. Hentschel, *Phys. Rev. A* **2008**, *78*, 053809.
- [20] S. Liu, J. Wiersig, W. Sun, Y. Fan, L. Ge, J. Yang, S. Xiao, Q. Song, H. Cao, *Laser Photonics Rev.* **2018**, *12*, 1800027.
- [21] Q. Song, Z. Gu, N. Zhang, K. Wang, N. Yi, S. Xiao, *Sci. China: Phys., Mech. Astron.* **2015**, *58*, 114210.
- [22] B. Redding, L. Ge, Q. Song, J. Wiersig, G. S. Solomon, H. Cao, *Phys. Rev. Lett.* **2012**, *108*, 253902.
- [23] J. Wiersig, A. Eberspächer, J.-B. Shim, J.-W. Ryu, S. Shinohara, M. Hentschel, H. Schomerus, *Phys. Rev. A* **2011**, *84*, 023845.
- [24] B. Peng, S. K. Özdemir, M. Lierter, W. Chen, J. Kramer, H. Yilmaz, J. Wiersig, S. Rotter, L. Yang, *Proc. Natl. Acad. Sci. USA* **2016**, *113*, 6845.
- [25] S. Özdemir, S. Rotter, F. Nori, L. Yang, *Nat. Mater.* **2019**, *18*, 783.
- [26] C. Strelow, C. Schultz, H. Rehberg, M. Sauer, H. Welsch, A. Stemmann, C. Heyn, D. Heitmann, T. Kipp, *Phys. Rev. B* **2012**, *85*, 155329.
- [27] X. Li, *Adv. Opt. Photonics* **2011**, *3*, 366.
- [28] F. Gu, F. Xie, X. Lin, S. Linghu, W. Fang, H. Zeng, L. Tong, S. Zhuang, *Light: Sci. Appl.* **2017**, *6*, e17061.
- [29] M. Pöllinger, D. O'Shea, F. Warken, A. Rauschenbeutel, *Phys. Rev. Lett.* **2009**, *103*, 053901.
- [30] J. M. Ward, Y. Yang, F. Lei, X.-C. Yu, Y.-F. Xiao, S. N. Chormaic, *Optica* **2018**, *5*, 674.
- [31] L. Ma, S. Li, V. Fomin, M. Hentschel, J. Götte, Y. Yin, M. Jorgensen, O. G. Schmidt, *Nat. Commun.* **2016**, *7*, 10983.
- [32] J. Wang, Y. Yin, Q. Hao, Y.-D. Yang, S. Valligatla, E. Saei Ghareh Naz, Y. Li, C. N. Saggau, L. Ma, O. G. Schmidt, *Nano Lett.* **2018**, *18*, 7261.
- [33] J. Wang, Y. Yin, Q. Hao, Y. Zhang, L. Ma, O. G. Schmidt, *Adv. Opt. Mater.* **2018**, *6*, 1700842.
- [34] Y. Yin, J. Wang, X. Lu, Q. Hao, E. Saei Ghareh Naz, C. Cheng, L. Ma, O. G. Schmidt, *ACS Nano* **2018**, *12*, 3726.
- [35] J. Wang, Y. Yin, Y.-D. Yang, Q. Hao, M. Tang, X. Wang, C. N. Saggau, D. Karnaushenko, X. Yan, Y.-Z. Huang, L. Ma, O. G. Schmidt, *ACS Photonics* **2019**, *6*, 2537.
- [36] D. Bachman, Z. Chen, C. Wang, R. Fedosejevs, Y. Y. Tsui, V. Van, J. Lightwave Technol. **2017**, *35*, 588.
- [37] A. Canciamilla, F. Morichetti, S. Grillanda, P. Velha, M. Sorel, V. Singh, A. Agarwal, L. C. Kimerling, A. Melloni, *Opt. Express* **2012**, *20*, 15807.
- [38] R. Henze, C. Pyrlak, A. Thies, J. M. Ward, A. Wicht, O. Benson, *Appl. Phys. Lett.* **2013**, *102*, 041104.

- [39] M. M. Milosevic, X. Chen, W. Cao, A. F. Runge, Y. Franz, C. G. Littlejohns, S. Mailis, A. C. Peacock, D. J. Thomson, G. T. Reed, *IEEE J. Sel. Top. Quantum Electron.* **2018**, *24*, 17594886.
- [40] J. Schrauwen, D. Van Thourhout, R. Baets, *Opt. Express* **2008**, *16*, 3738.
- [41] Y. Shen, I. B. Divlansky, D. N. Basov, S. Mookherjea, *Opt. Lett.* **2011**, *36*, 2668.
- [42] E. I. Moiseev, N. Kryzhanovskaya, Y. S. Polubavkina, M. V. Maximov, M. M. Kulagina, Y. M. Zadiranov, A. A. Lipovskii, I. S. Mukhin, A. M. Mozharov, F. E. Komissarenko, Z. F. Sadrieva, A. E. Krasnok, A. A. Bogdanov, A. V. Lavrinenko, A. E. Zhukov, *ACS Photonics* **2017**, *4*, 275.
- [43] M.-K. Seo, H.-G. Park, J.-K. Yang, J.-Y. Kim, S.-H. Kim, Y.-H. Lee, *Opt. Express* **2008**, *16*, 9829.
- [44] Y. Fang, S. Li, Y. Mei, *Phys. Rev. A* **2016**, *94*, 033804.
- [45] J. Wnuk, S. Rosenberg, J. Gorham, W. Van Dorp, C. Hagen, D. Fairbrother, *Surf. Sci.* **2011**, *605*, 257.
- [46] A. Remenyuk, T. Zvonareva, I. Zaharova, V. Tolmachev, L. Belyakov, T. Perova, *Semiconductors* **2009**, *43*, 915.
- [47] J. Wang, Y. Yin, Q. Hao, S. Huang, E. Saei Ghareh Naz, O. G. Schmidt, L. Ma, *ACS Photonics* **2018**, *5*, 2060.
- [48] S. G. Johnson, M. Ibanescu, M. A. Skorobogatiy, O. Weisberg, J. D. Joannopoulos, Y. Fink, *Phys. Rev. E* **2002**, *65*, 066611.
- [49] J. Stathis, M. Kastner, *Phys. Rev. B* **1987**, *35*, 2972.
- [50] A. Li, W. Bogaerts, *Laser Photonics Rev* **2019**, *13*, 1800244.
- [51] E. T. Arakawa, M. W. Williams, T. Inagaki, *J. Appl. Phys.* **1977**, *48*, 3176.
- [52] T. Kipp, H. Welsch, C. Strelow, C. Heyn, D. Heitmann, *Phys. Rev. Lett.* **2006**, *96*, 077403.